From indoor exposure to inhaled particle deposition: A multiphase journey of inhaled particles

Kiao Inthavong (✉)

School of Engineering, RMIT University, PO Box 71, Bundoora, 3083, Australia

Abstract

Indoor air quality and its effect on respiratory health are reliant on understanding the level of inhalation exposure, particle inhalability, and particle deposition in the respiratory airway. In the indoor environment, controlling airflow through different ventilation systems can reduce inhalation exposure. This produces a wide variety of complex flow phenomena, such as recirculation, coanda flow, separation, and reattachment. Airborne particles drifting through the air, that move within the breathing region become inhaled into nasal cavity the nostrils. Studies have developed the aspiration efficiency to assist in predicting the fraction of inhaled particles. Inside the nasal cavity, micron and submicron particle deposition occurs in very different ways (inertial impaction, sedimentation, diffusion) and different locations. In addition, fibrous particles such as asbestos are influenced by tumbling effects and its deposition mechanism can include interception. Indoor fluid–particle dynamics related to inhalation exposure and eventual deposition in the respiratory airway is presented. This study involves multi-disciplinary fields involving building science, fluid dynamics, computer science, and medical imaging disciplines. In the future, an integrated approach can lead to digital/in-silico representations of the human respiratory airway able to predict the inhaled particle exposure and its toxicology effect.

1 Introduction

The convergence of fluid dynamics, computer science, and medical imaging disciplines has produced a multi-disciplinary field of computational modelling of the human respiratory airway. By introducing a second phase to the inhaled air, and multi-physics (e.g., heat transfer, dynamic meshing), the modelling capabilities increase and provide opportunities for new applications. The human nasal cavity is the primary route for connecting the air we breathe through our nostrils. Experimental and computational multiphase studies exploring the relationship between airway geometry, flow phenomena, and physiology lead to a better understanding of the consequences of both intentional (drug delivery) and unintentional (inhalation toxicology) inhalation exposure to particles and droplets in the air. The primary objective of such studies is predicting dosimetry of the inhaled particulate matter, which is influenced by the nasal anatomy, and interactions with the mucus.

Figure 1 shows the different stages required for obtaining the eventual dosimetry from either inhalation exposure or drug delivery. For example the dosimetry from inhalation exposure can be calculated as

$$\eta_{\text{exposure}} = \alpha_{1a} \times \alpha_2 \times \alpha_3 \times \alpha_4 \tag{1}$$

where α is the concentration fraction at each stage, and subscripts are: 1 = airborne concentration obtained by aerosol sampling, 2 = aspiration efficiency through the nostrils, 3 = deposition flux on the mucous surface, and 4 = mucociliary clearance rate. To obtain concentration fractions at each particle transport stage, studies have investigated: (i) inhalation exposure or drug delivery, (ii) particle deposition flux in the nasal cavity surface, and more recently (iii) particle penetration through the mucus. These individual studies can be integrated to include pulmonary system where drug delivery from a medical device or airborne particles is tracked down to the lungs. This provides an integrated, comprehensive analysis and a holistic view of cause–effect therapeutic or toxicology assessment.

This review brings to date the activities of particle inhalation in both toxicology and therapeutic context, and the recent advances in technology that will drive future
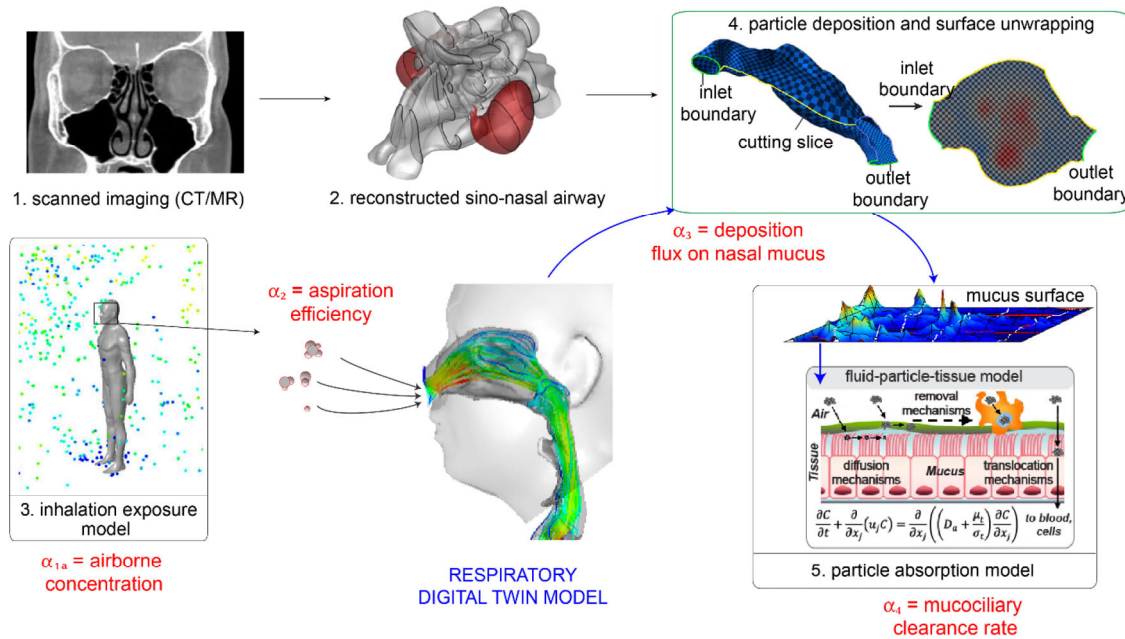
Fig. 1 Integrated computational modelling for a respiratory digital twin capable of evaluating inhaled particle dosimetry.

trends and research activity. Techniques and results that have been established to obtain concentration fractions are reviewed, and the current challenges are discussed which aim to foster new future directions to address the shortcomings of the current state-of-the-art.

2 Inhalation exposure

2.1 Indoor inhalation exposure

Inhalation of toxic airborne contaminants such as asbestos and airborne pollutants is a frequent occurrence for those working in the manufacturing and processing industries. While in public spaces, e.g., office spaces, lecture theatres, public transport, airborne contagions such as influenza viruses can be quickly spread. Computational studies have shown that airflow patterns are influenced by furniture layout

(Cheong and Djunaedy, 2001) and this affects aerosol dispersion (Whicker et al., 2002). Additionally, control of airflow direction in buildings and use of negatively pressurized isolation rooms reduced the spread of diseases in hospitals (Luongo et al., 2016). Since the contaminant source and its trajectory in the surrounding environment are paramount to the likelihood of inhalation, predictions of the air phase must be reliable.

Controlling airflow can be influenced by diffuser ventilation systems which produce a wide variety of complex flow phenomena. Recirculation, coanda flow, separation, and reattachment are some of the flow characteristics that can be found in a room (Fig. 2). Flow velocities can also vary considerably with high-velocity wall jets at the diffusers and low velocities in the free stream region of a room for occupant comfort. These flow characteristics exert significant influence on the distribution of contaminant particles
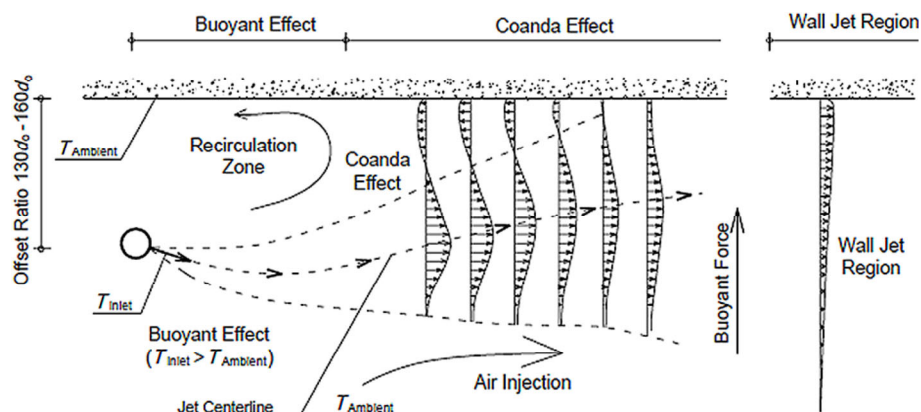

Fig. 2 Image of indoor flow phenomena caused by diffuser, e.g., jet flow.

suspended in the air and therefore the accurate prediction of such airflows plays an important role in the design process of ventilation systems for both occupant comfort and contaminant removal.

Due to the lower computational effort most airflow simulations are based on the Reynolds Averaged Navier Stokes (RANS) equations with a first-order-closure turbulence model. Chen's (1995) early computational study recommended the RNG k–ε model for simulations of indoor airflow as it was slightly better than the standard k–ε model. This was confirmed later in Zhang et al. (2007), where the RNG k–ε and v^2–f models were the best overall performing models in the four cases studied. Nielsen et al. (1998) later reported that a low Reynolds number k–ε model was required for transport processes that occurred close to surfaces or stratification cases, due to the damping effect of buoyancy.

To improve flow predictions in RANS models, nonlinear eddy viscosity turbulence models were developed calibrated to the normal stresses (Heschl et al., 2013, 2014). The calibration ensured the log-law, and shear-layer behaviour was correct. In addition, the nonlinear eddy viscosity model reproduced the anisotropic Reynolds stresses and consequently turbulence-driven secondary motions. Future studies could further calibrate nonlinear eddy viscosity models to different classes of indoor airflows.

Simulations of indoor particle dispersion introduce the challenge of fluid–particle turbulence, which is modelled through either the Eulerian or Lagrangian method. The Eulerian method is useful for studying particle concentration distributions in indoor flows especially when dealing with diffusional parameters (Murakami, 1992). It treats the flow as a single fluid, where the particle phase is described as a modified scalar species, with a concentration value. This makes the Eulerian method easy to solve and implement, and has been widely used (Holmberg and Chen, 2003). The particles are treated as a continuum and this is often referred to as a single fluid (or mixture) model as

$$\frac{\partial \rho C}{\partial t} + \frac{\partial}{\partial x_i}\left(\rho \overline{u}_i C - \Gamma \frac{\partial C}{\partial x_i}\right) = S_c \qquad (2)$$

where t is the time, C is the particle concentration, ρ is the density of air, $x_i (i=1,2,3)$ are the three coordinates, $\overline{u}_i$ is the averaged air velocity components in the three directions, and Γ is the effective particle diffusivity. S_c is the particle source term which is used when the relative motion between fluid and particle phase is significant and is termed the "drift flux" component. This is typically used for particles greater than 5 μm, where drift term becomes significant.

When RANS turbulent models are used to account for turbulent flows, there is an assumption of homogeneous turbulence in the flow field, but in reality, this is not necessarily

the case. In the freestream, this is not as important, but in the near-wall region where highly anisotropic behaviour occurs, RANS models fail to capture the physics sufficiently, and in particular, has a compounding effect on particle deposition onto surfaces. For the Eulerian mixture model, a deposition submodel is required to account for the Eulerian description of particle deposition onto surfaces (Lai and Nazaroff, 2005; Chen et al., 2006).

The alternative approach is the Lagrangian method that treats the particle as a secondary dispersed phase, where individual particles are traced through the indoor environment using Newton's law of motion, $\sum F = 0$. The method tracks a large number of individual particles through small time steps through

$$\frac{\partial \vec{u}_p}{\partial t} = F_D\left(\vec{u} - \vec{u}_p\right) + \frac{\vec{g}\left(\rho_p - \rho\right)}{\rho_p} + F_c \qquad (3)$$

where $\vec{u}$ is the velocity vector, $\vec{g}$ is the gravity acceleration, ρ is the density, F_D is the drag force, and F_c is the additional source term. The subscript p represents the particle. The performance of the Lagrangian method is very sensitive to the predicted mean flow and turbulence, particularly near walls. The strict requirement for resolving the near-wall flow in turbulent flows challenges the modelling capability of many RANS models. The anisotropic behaviour produces a much smaller fluctuation in the normal to the wall direction, v'. The fluctuating velocities are decomposed from $\sqrt{2k/3} = v' = u' = w'$, where k is the turbulent kinetic energy. This error propagates to the Lagrangian particle tracking when dealing with the turbulent dispersion, and leads to higher deposition of smaller inertial particles. Since this issue affected the smaller inertial particles, Inthavong et al. (2006) switched off the turbulent dispersion for particle deposition with inertial parameter less than < 10,000, equivalent to a particle with a diameter of $d_p \approx 5.5$ μm for a flow rate of 20 L/min. Liu et al. (2007) showed that by damping the turbulent kinetic energy, and therefore damping the v' component, in the near-wall region, predictions of the deposition efficiency improved; while Inthavong et al. (2011b) evaluated the v' component directly by taking its profile from the $v^2 - f$ turbulence model to improve the particle deposition (Fig. 3). The $v^2 - f$ model (Zhang and Chen, 2009; Li and Gong, 2012; Heschl et al., 2013) has been popular, among the RSM and LES methods (Liu and Novoselac, 2014) as alternatives to indoor airflow modelling to serve as work arounds to resolve the strong anisotropic behaviour in the near-wall region. Recently the continuous random walk model has been applied to include the effect of turbulent fluctuations on particle trajectories which is based on the normalized Langevin equation (Dehbi, 2011; Ghahramani et al., 2014).

(a)

(b)
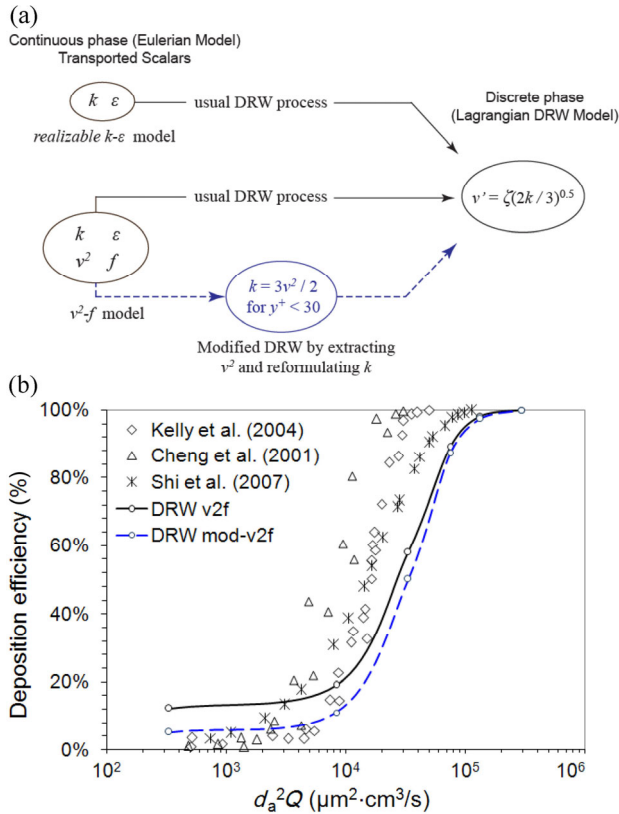
Fig. 3 (a) Comparisons of the inertial particle deposition simulation using the DRW models with the v^2–f turbulence model, against experimental data. (b) Schematic of the Lagrangian DRW model process for both the k–ε and the v^2–f turbulence models. Both models still produce an over predicted normal fluctuating velocity v'. A modification to the DRW is shown by the dashed blue line which forces the DRW to use v^2 to calculate the v' component in the near-wall region (Inthavong et al., 2011b; reproduced with permission © Elsevier Ltd. 2011).

2.2 Aspiration efficiency

Airborne particles (transported by indoor air movements) that move within the breathing region are drawn into the nostrils. This can be viewed as a form of aerosol sampling, and therefore the concept (borrowed from sampling aerosol studies) of aspiration efficiency can be used. This is defined as the ratio of particle concentration entering a sampling inlet to the particle concentration at an undisturbed upstream location (Belyaev and Levin, 1972). For human inhalation this can be directly applied as the inhaled particle concentration (C_i) to the undisturbed freestream particle concentration (C_o):

$$AE = C_i / C_o \qquad (4)$$

The inhaled concentration C_i can be expressed as the number of particles inhaled (N_i) per volume of air, $A_i V_i t$:

$$C_i = \frac{N_i}{A_i V_i t} \qquad (5)$$

where A_i is the inhalation area, V_i is the average inhalation velocity, and t is the time.

Experimental and numerical studies assume a uniform particle concentration upstream of the manikin as the velocity field is unaffected by the presence of the body. The aspiration efficiency was measured experimentally for different particle sizes, wind velocities, and breathing patterns with stationary humanoid models and an on-coming wind (Aitken et al., 1999; Nazaroff, 2008). Kennedy and Hinds (2002) established empirical correlations to describe the orientation-averaged aspiration efficiency as a function of particle diameter for wind velocities ranging from 0.4 to 1.6 m/s. Baldwin and Maynard (1998) showed that indoor ambient airflow velocities were much lower ranging between 0.1 and 0.4 m/s. Experimental measurements in wind tunnels are challenging to maintain constant airflows and maintaining uniform upstream concentrations of large particles travelling through the domain, due to gravitational settling (Dai et al., 2006).

CFD simulations provide the ability to control the upstream flow velocities and concentrations. Anthony and Flynn (2006) evaluated the aspiration efficiency through the mouth, combining facing the wind (0.2, 0.4 m/s) orientation with constant inhalation (1.8, 4.3 m/s) for particles in the range of 0.3–116 μm. Subsequent work followed, with a focus on: effect of facial features (Anthony, 2010); airflow/wind orientation effects (Anthony and Anderson, 2013); secondary aspiration due to particle rebound (Anderson and Anthony, 2014). Their body of work culminated in an empirical correlation for human aspiration through the mouth in low-oncoming (facing-the-wind) velocity air accounting for particle size, freestream velocity, and breathing velocity (or rate) given as

$$\begin{aligned} AE = 1.01 - 3.58{\times}10^{-5}d_{ae}^2 - 0.005d_{ae} + 2.5{\times}10^{-4}(d_{ae} \times U_s) \\ - 0.79\,(U_o/U_s) \qquad (6) \end{aligned}$$

where d_{ae} is the aerodynamic diameter, U_s is the breathing velocity, and U_o is the freestream velocity of an on-coming flow.

King Se et al. (2010) presented computational modelling of aspiration efficiency through the nose and compared it with oral inhalation of airborne particles. By tracing its trajectories back to the upstream release location, the initial particle source region was determined. The aspiration efficiency curve for oral breathing was compared with literature, and a new correlation was proposed for aspiration efficiency through the nose (Fig. 4).

Li et al. (2012) calculated the flow field in the indoor environment and established inhalation velocity profiles at the nostrils which were neither uniform nor a symmetric parabolic/blunt profile. The velocity profiles at the nostrils were then transferred to a human nasal cavity model as
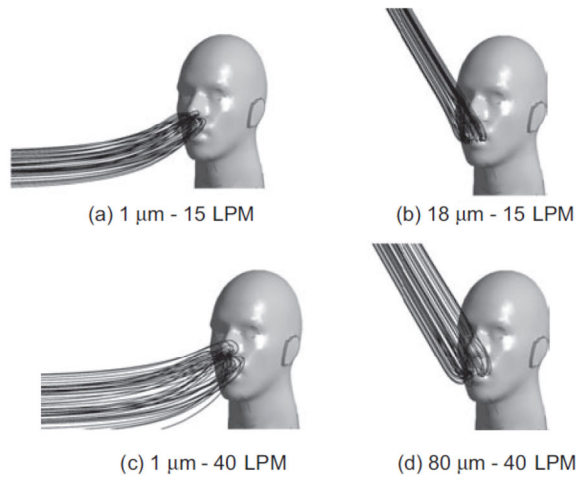
Fig. 4 Particle trajectory paths for 1 and 18 μm particles at an inhalation flow rate of 15 LPM (litres per minute) and 1 and 80 μm particles at an inhalation flow rate of 40 LPM with an oncoming free stream of U_o = 0.20 m/s (King Se et al., 2010; reproduced with permission © Taylor & Francis 2010).

inlet boundary conditions for a separate particle inhalation study (Fig. 5).

Since the particle motion is governed by a form of ordinary differential equation (Eq. (3)), a solution can be found if some simplifications are applied. If the drag coefficient is kept constant, as $C_d = 24/Re$ is kept constant and $\vec{u} = u_o$ as a fixed ambient flow, the solution becomes:

$$x = x_o + U_\infty t - U_\infty \tau \exp\left(-\frac{t}{\tau}\right)$$

$$y = y_o + V_\infty \tau + (g\tau^2 + V_\infty \tau)\exp\left(-\frac{t}{\tau}\right)$$

$$- g\tau^2 + t(V_\infty + g\tau)$$

(7)

where U_∞ can be 0.05, 0.20, or 0.35 m/s for the horizontal free-stream velocity, while V_∞ is zero. The variables x_o and y_o are the initial particle locations at time $t = 0$ s, g is the gravity, and τ is the particle relaxation time. The downfall of this simplified solution is the uniform free-stream velocity assumption which does not account for changes in the velocity field, particularly in the vicinity of the human body and face. Instead, numerical integration using a Runge–Kutta scheme can be used to track the particles. Figure 6 shows a single representative trajectory for 1, 10, 40, and 80 mm particles.

The particles are released from different upstream plane locations of 20, 50, and 100 cm from the nose tip to investigate the trajectories and to determine if the particle
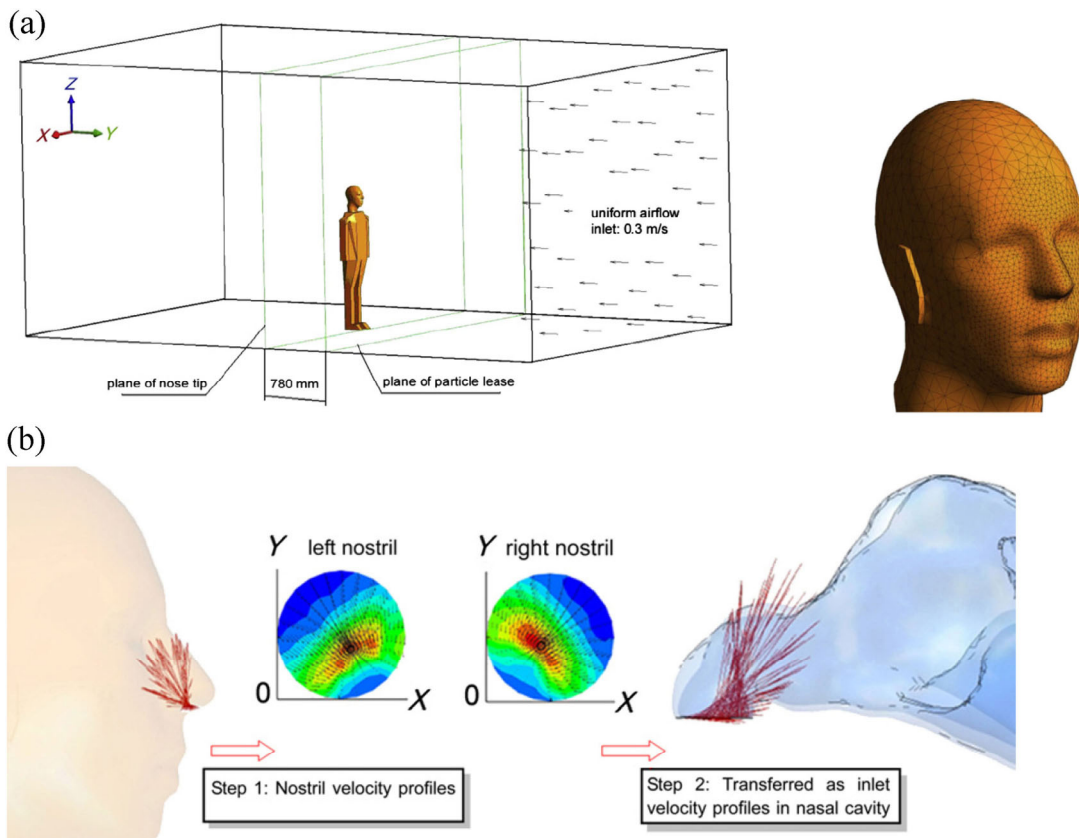

Fig. 5 (a) Indoor airflow simulation to establish the outlet velocity profiles at the nostrils. (b) These profiles were subsequently transferred to a human nasal cavity model for particle deposition studies, where velocity components u, v, w taken from the nostril outlet in the room simulation to the nostril inlets in the internal nasal cavity simulation (Li et al., 2012; reproduced with permission © Elsevier Ltd. 2011).

TSINGHUA UNIVERSITY PRESS Springer

trajectory is consistent for different upstream source locations. The trajectories are overlaid onto the free-stream velocity vectors in the plane which indicates the potential influence of the surrounding air on the particle transport. The coordinates have the origin $(x, y) = (0, 0)$ located at the nostrils and therefore the trajectories of the inhaled particles will all converge to the origin.

Determining the dosimetry due to exposure to a contaminant source can therefore, be predicted either by Eq. (6) or the aspiration efficiency curves found in Fig. 7 from King Se et al. (2010).

2.3 Wake effects of aspiration efficiency

Wake flows in the indoor environment are created from flow separation over bluff bodies, including human bodies. It is characterised by a mixing zone of vortices entraining the air into a recirculating flow proximal to the body. The flow disturbs airborne particles and also lifts/redisperses settled particles from the floor, enhancing pollutant exposure. Early studies of human-induced wake flows (Kim and Flynn, 1991; Kulmala et al., 1996) visualised boundary layer separation and the size and location of the wake region in
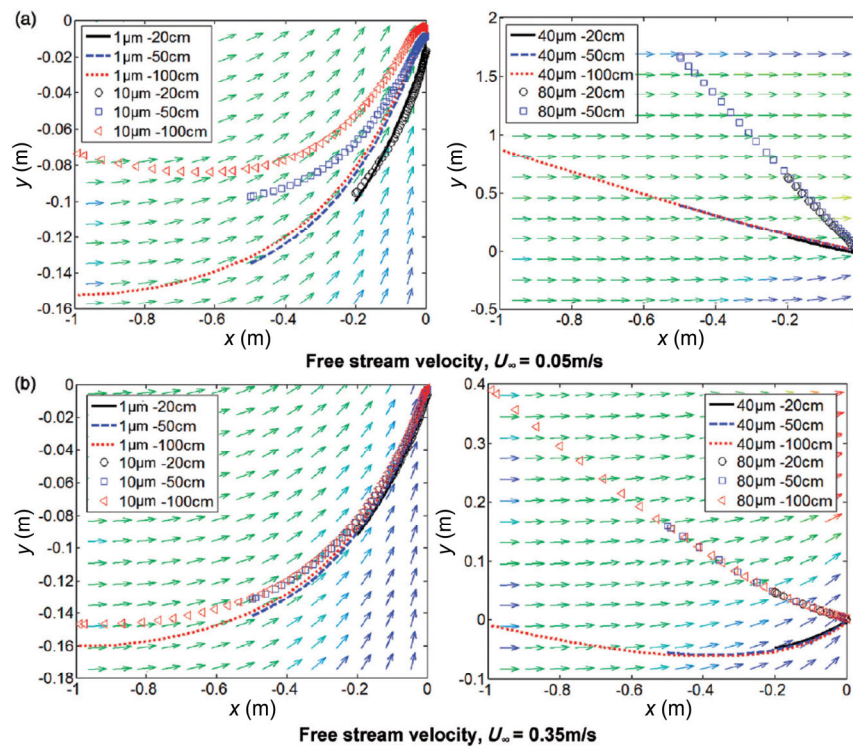
Fig. 6 Particle trajectories represented by symbols (10 and 80 μm) and lines (1 and 40 μm) released from different upstream distances away from the nostrils in the *x*-axis, and at free-stream velocities of (a) $U_\infty = 0.05$ m/s and (b) $U_\infty = 0.35$ m/s. Velocity vectors in the background represent the ambient flow field, coloured by its magnitude with red being the peak velocity and blue the minimum velocity (Inthavong et al., 2013a; reproduced with permission © Taylor & Francis 2013).
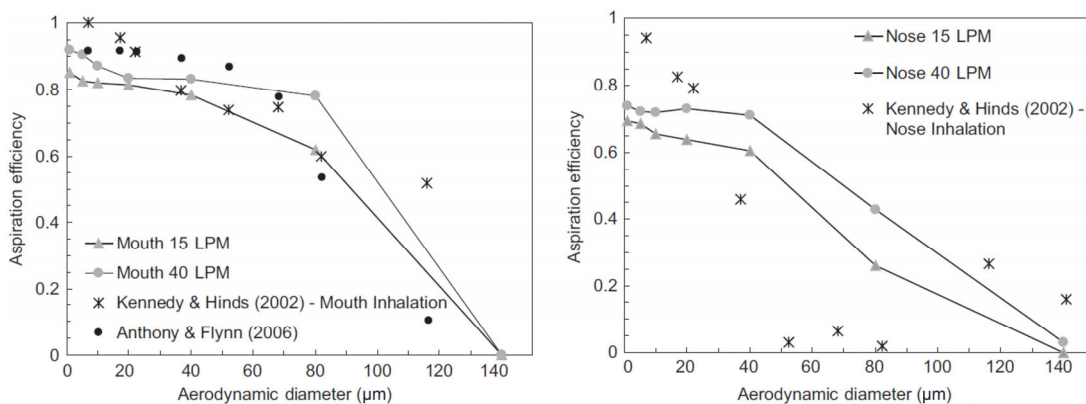
Fig. 7 Aspiration efficiency for mouth and nose inhalation under facing the wind condition (Inthavong et al., 2013a; reproduced with permission © Taylor & Francis 2013).

a wind tunnel.

Steady flow over a stationary manikin neglects any flow disturbance caused by the manikin acceleration and deceleration, which fails to represent the effects of human motion during walking cycles. The impact of a moving manikin through idle air on contaminant transport provides challenges experimentally. This is partly due to the flow visualisation techniques that are designed to measure a moving fluid. For example, traditional smoke visualisation methods involve an alkane chemical such as mineral oil evaporating off a heated smoke wire and allowed to streak through moving air in a wind tunnel. However, this would not work for a moving manikin in a still environment due to complexity in setup and operation.

To overcome this, a new technique to visualise the wake flow induced by a moving human manikin was proposed in Inthavong et al. (2017). Smoke was generated from the chemical reaction between a saturated chamber of acetic acid (CH_3COOH) and a manikin dabbed with cyclohexylamine ($C_6H_{11}NH_2$) that produced a salt (ethanoate) as the manikin moved through the chamber (Fig. 8). This provided the ability to visualise the wake development during the manikin motion and after the manikin comes to a stop. High-speed photography was used to capture the transient wake flow development in detail.

In terms of computational modelling, Poussou et al. (2010) studied the flow and contaminant transport in an airliner cabin induced by a moving body represented by a rectangular block. The results showed strong intermittency in the instantaneous near-wake flow and a symmetric downwash flow was observed along the vertical centreline of the moving body. Oberoi et al. (2010) investigated a human walking through a room, stopping, and then walking in place, causing particles to be re-suspended from a carpet. The results predicted particle re-suspension rates induced by human motion, but further work in modelling the fine-scale details of the re-suspension was suggested.

Wang and Chow (2011) found that a faster human walking speed could effectively reduce the transport or dispersion of suspended cough droplets. The effect of the human manikin motion was confirmed by Choi and Edwards (2012) who used an immersed boundary method and found reduced mass transport from a contaminated room moving into a cleanroom from faster walking speeds, and from Tao et al. (2017a) who showed that higher walking speed reduced exposure to contaminants in the breathing region. Tao et al. (2017a) used a dynamic mesh method to move a manikin through an indoor environment to investigate the human-induced wake and particle dispersion under three walking speeds. The results showed an upward-
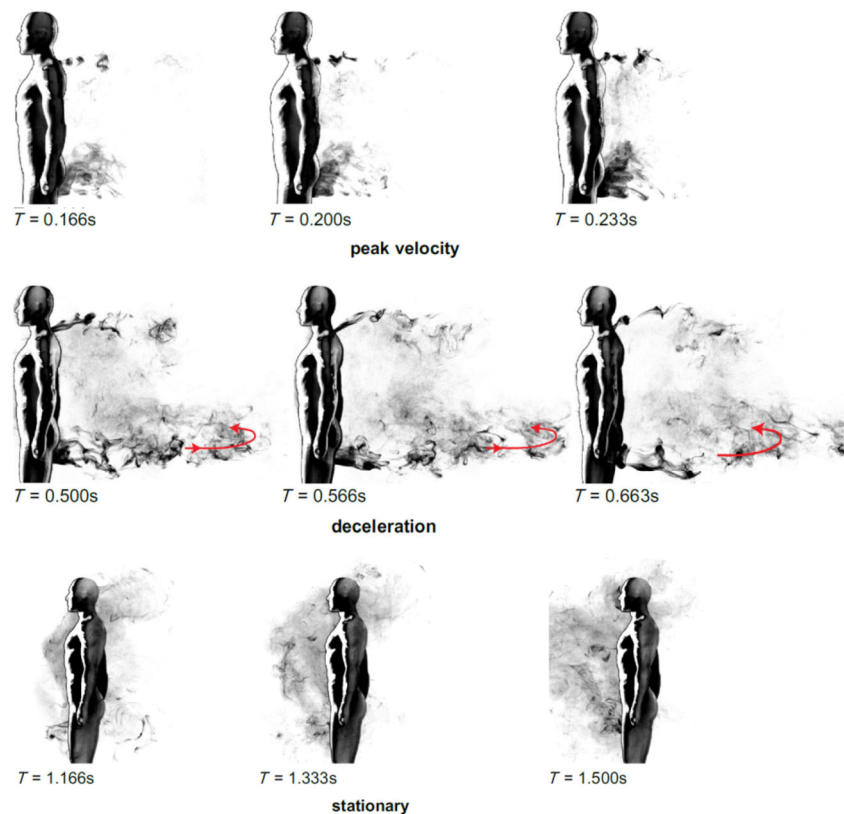
Fig. 8 Different flow separation produced as a manikin moves through quiescent air, decelerates, before coming to a stop (Inthavong et al., 2017; reproduced with permission © The Visualization Society of Japan 2016).

TSINGHUA UNIVERSITY PRESS   Springer

directed flow in front of the body combined with a high velocity downward-directed flow at the rear of the body. There was also a stagnant region behind the gap between the legs and counter-rotating vortices in the wake region.

Simplified geometries such as vertical finite cylinders and cuboids used as substitutes for human bodies (Thatcher et al., 2004; Poussou et al., 2010) produce discrepancies in the flow behaviours due to the simplified geometry. For example, when legs are considered as two cylinders instead of a cylindrical block, there is increased mixing in the wake produced by the gap between the legs accelerating flow (Edge et al., 2005). Advanced modelling of a moving manikin with realistic walking motion (swinging arm and leg), and heat transfer was performed (Tao et al., 2017b, 2017c). Walking postures were simplified and the arms and legs were treated as rigid swinging pendulums with its pivot taken at the shoulder and hips 60° and 40°, respectively.

Figure 9 shows velocity contours and vectors on the mid-plane ($x = 0$ m) and at the plane through the right leg ($x = 0.06$ m) under a rigid and swinging motion at different time steps. The induced velocities were created from the relative motion between stationary and fixed stagnant fluids. In the upper body, this is evident from the high velocities along the body and a trailing wake forms. Vectors show the fluid moves upwards and around in a semi-circle from the head returning into the wake as it becomes entrained into the flow. Velocity vectors in the wake move back into the wake towards the manikin. In the front of the body the vectors are directed forwards suggesting that the fluid is pushed away as the body moves through the flow field. The velocity contours on the right leg at plane ($x = 0.06$ m) shows high velocity at the gap between the arm and body. This suggests high velocities are formed at separation regions around the body through the relative motion of the moving body.

The thermal plume emanating from a manikin influenced the flow field (Murakami, 2004), and the particle trajectory near stationary manikins (Li et al., 2012). However, the influence of the moving manikin introduces advective influences that reduce the production of a thermal plume.

The effect of walking on the thermal plume is shown in Fig. 10 for a walking manikin with swinging limb motion. The thermal environment around the body under steady state was first established. A thermal plume was formed where it was weak at the bottom of the body and became stronger in the upper body. The plume rose vertically above the manikin head with a maximum velocity of 0.25 m/s at 0.18 m above the head. As the manikin moved, the thermal plume remained and trailed behind slowly remaining connected to the manikin. The velocity vectors in the thermal plume are directed upwards and nearby flow is entrained in the plume.

The effect of manikin motion on particle redispersion is shown in Fig. 11 where a higher walking speed produced stronger downward airflow in the front of the body, preventing re-suspension of floor particles from rising to the upper body regions. The upper body produced upward flow in front of the body which caused particles to rise quickly into the breathing zone. At the back of the upper body a strong downwash was formed and caused particles to almost stick to the back of the body while the manikin was moving. Although a lower walking speed at 0.8 m/s would cause smaller turbulent flow, particles were continuously transported to the upper region due to the longer fluid–particle interaction and residence time for particle exposure, and more upwards velocities in the wake structure. A faster-moving manikin produced greater downward forces near the floor. Additionally, the interaction time between the

(a) centre plane $x = 0$ m
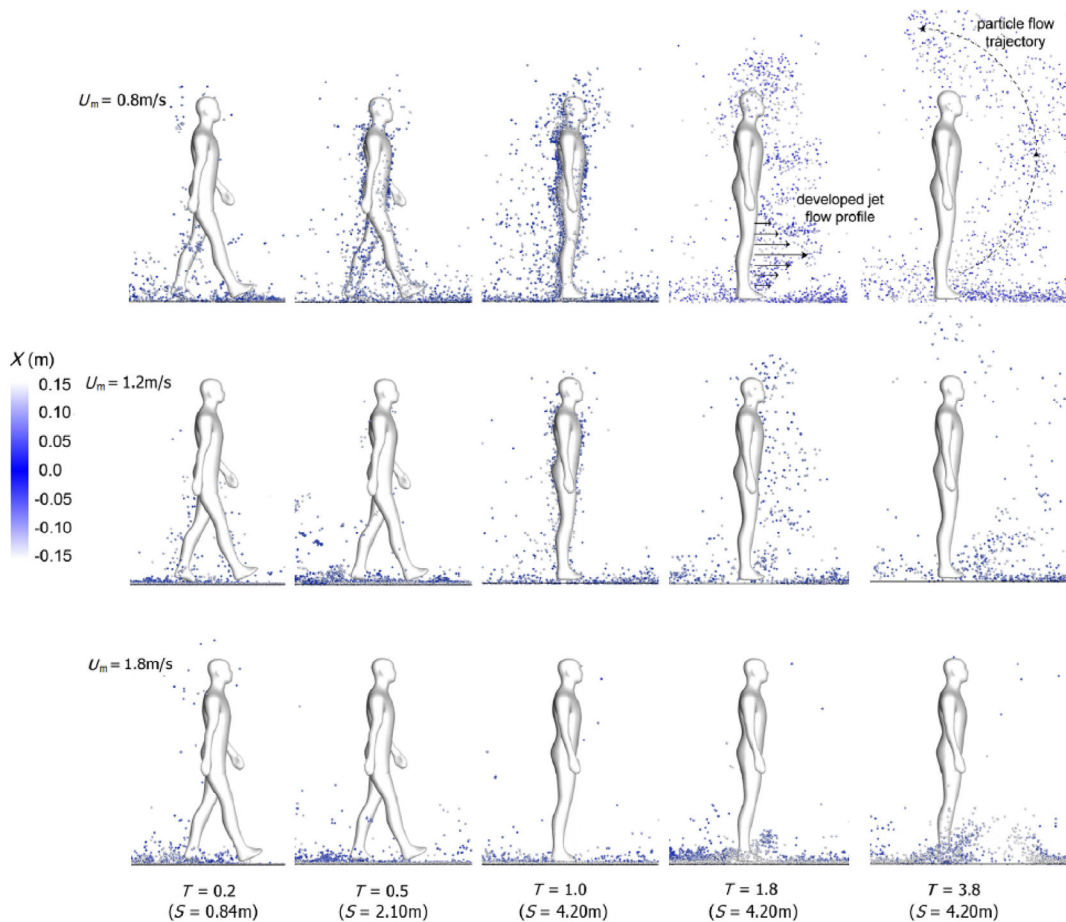
(b) off-centre plane $x = 0.06$ m
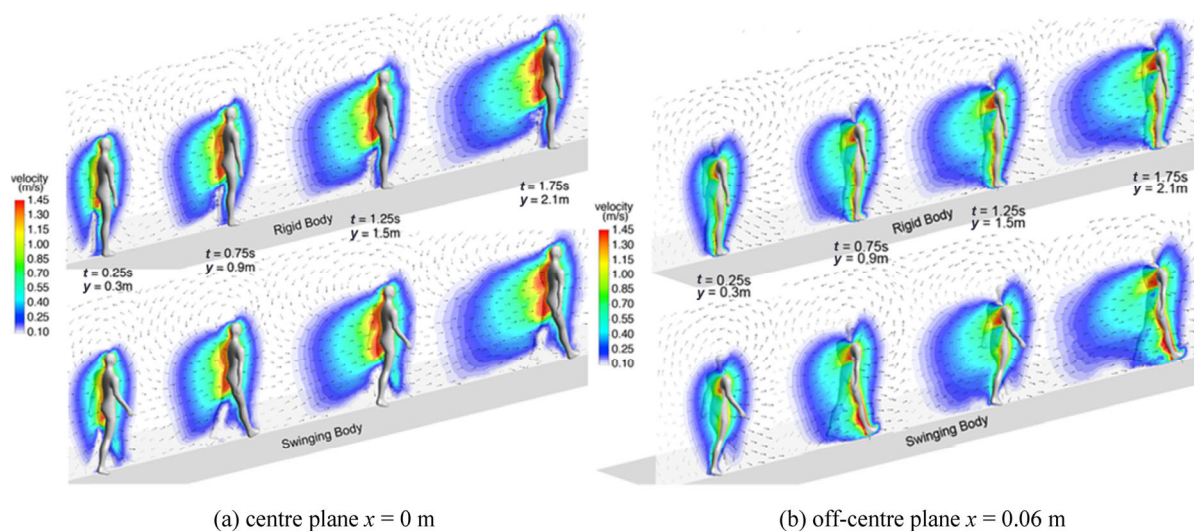
Fig. 9 Velocity contours produced from a manikin with swinging limbs (Tao et al., 2017c; reproduced with permission © Elsevier Ltd. 2017).
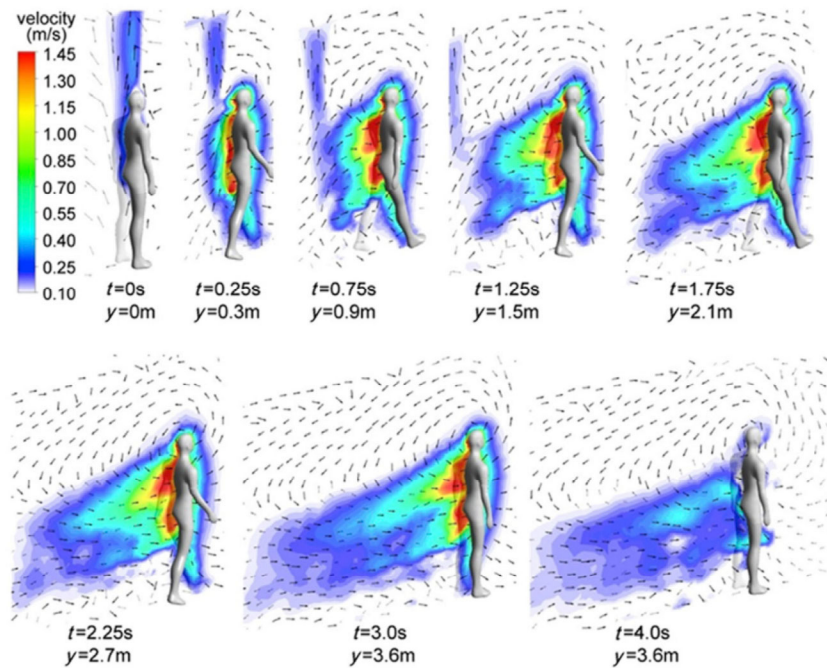
Fig. 10 Velocity field on the mid-plane (x = 0 m) under the thermal conditions at t = 0 s to t = 4.0 s (Tao et al., 2017c; reproduced with permission © Elsevier Ltd. 2017).

Fig. 11 Visualisation of particle redispersion caused by the walking manikin (from T = 0.2 (travelled 0.84 m) to T = 1.0 (travelled 4.2 m)) and after the manikin has stopped walking (from T = 1.0 to T = 3.8). The walking speed was U_m = 0.8 m/s, U_m = 1.2 m/s, and U_m = 1.8 m/s and the total travelled distance was S = 4.2 m (Tao et al., 2017b; reproduced with permission © Elsevier Ltd. 2017).

TSINGHUA UNIVERSITY PRESS   Springer

moving manikin and the surrounding air is much shorter for the faster moving manikin so the concentration at the same position was lower.

3   Inhaled particle deposition

3.1   Micron particle deposition

Individual aspects of the nasal cavity such as the geometry and flow rate collectively affect the airflow patterns and consequently, the transport of particles through the cavity. Significant anatomical factors include the nasal length, the bend from the nostrils into the cavity (Inthavong et al., 2011a, 2013a, 2019), and turbinate structure (Churchill et al., 2004). Xi et al. (2016) showed that the nostril inlet orientation has significant influence on eventual particle deposition, as it is the first point of interaction between the inhaled particles and the internal nasal anatomy. Doorly et al. (2008), Taylor (2010), and Shang et al. (2015b) corroborate the influence of the nostril orientation by including the outer face geometry. Figure 12 shows the extent of outer breathing zone influence.

Micron particle deposition in the nasal cavity is primarily due to inertial impaction and to a lesser extent, gravitational sedimentation and interception (Fig. 13). Deposition by interception becomes important for fibres due to its elongated shape and occurs when a particle travels close enough to a surface of the airway passages,

and an edge of the particle touches the surface. Deposition by interception is usually low due to the differences in dimensional magnitudes—fibre length $\approx 10^{-6}$ compared with airway geometry $\approx 10^{-3}$. Gravitational sedimentation is also less dominant as it requires that the particle is settling in the airway due to an absence of convective flow in the gas phase. For micron ranged particles, typically larger than 1 μm, the effects of particle inertia become important, and deposition is dominated by inertial impaction.

Inertial impaction occurs due to the particles not being able to follow the air streamlines, instead continuing more tangentially and depositing on the near wall. The inertial impaction parameter is used to define the particles impactability and is given as

$$I = d_{ae}^2 Q \tag{8}$$

where d_{ae} is the aerodynamic equivalent diameter in micron and Q is the flow rate usually taken with unit of cm³/s. Figure 14 shows the inertial parameter for particle deposition in a nasal cavity model with the external face, and without the face, where the deposition efficiency varied within the range 1.5×10^4 to 10^5.

3.2   Connecting aspiration efficiency and regional particle deposition

An integrated model connecting the upper respiratory airway with a human body (Inthavong et al., 2012) and
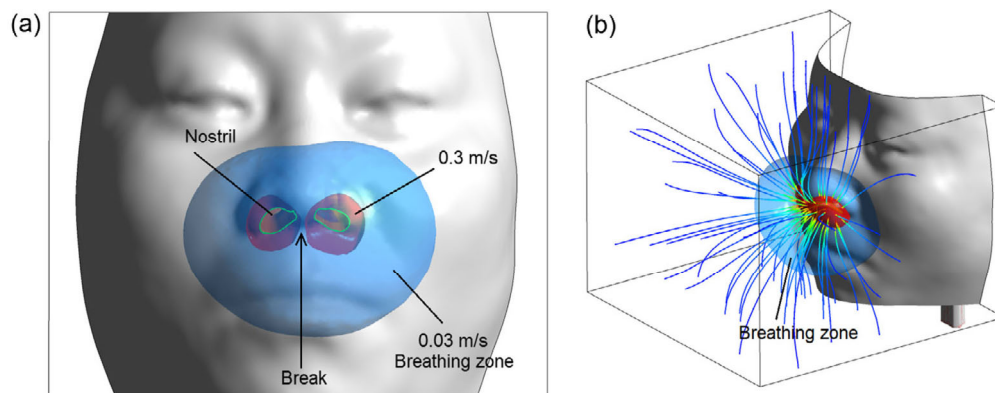
Fig. 12   Visualization of fluid velocities (a) by two iso-surfaces indicating the "critical velocity" 0.3 m/s and the boundary of the breathing zone (0.03 m/s) in the front view, (b) by flow streamlines coupled with iso-surface contours (Shang et al., 2015b; reproduced with permission © Elsevier Ltd. 2015).

inertial impaction   sedimentation   interception
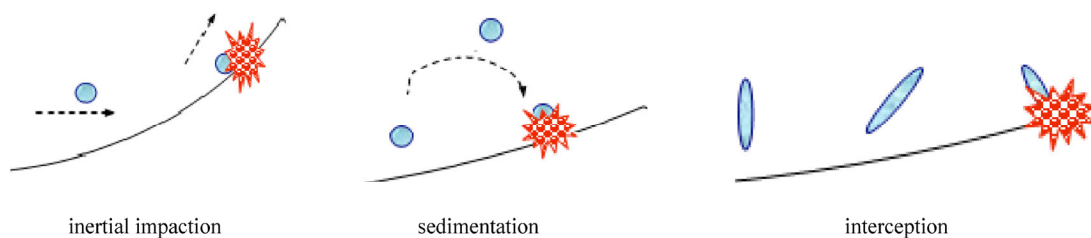
**Fig. 13**   Particle deposition mechanisms.
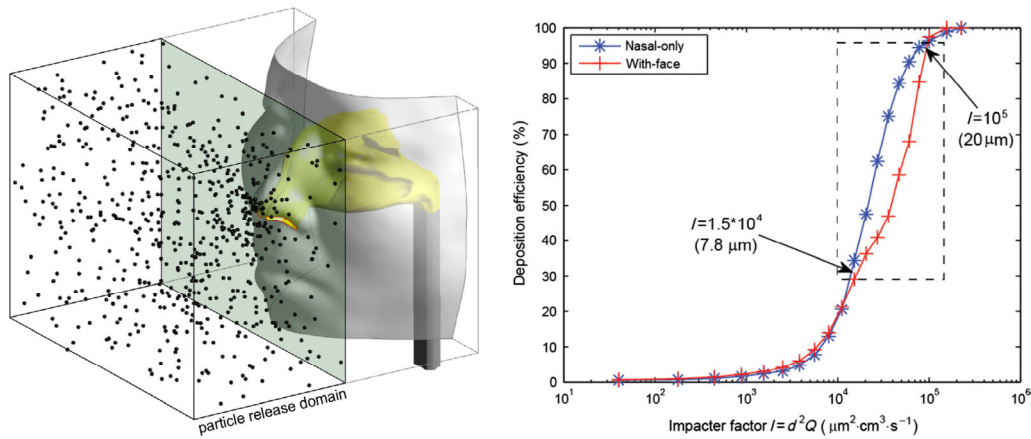
Fig. 14 Representation of discrete particle release locations for the "with-face" model. 10^5 particles were released throughout the external domain uniformly (Shang et al., 2015b; reproduced with permission © Elsevier Ltd. 2015).

placed inside a room, facing different airflow speeds (0.05–0.35 m/s) is shown in Fig. 15. The results in Fig. 16 showed flow streamlines diverge as it approached the human body, at the torso and accelerated upwards past the face and head before separating at the rear of the head, forming recirculating regions in the wake behind the body. Inhaled particles were tracked backwards to determine its origins. At a plane upstream from the face the locations of particles inhaled form a region known as the critical area. Its shapes were determined by reverse tracking the particles to its origins and colour coding their positions to determine

if a pattern could be deduced for predictions of local respiratory region deposition, which found that only the 15 μm particles produced a discernible pattern (Fig. 17). The results establish a better understanding of the relationship between particle inhalability and the eventual deposition in the respiratory airway.

3.3   Non-spherical particle deposition

The deposition of non-spherical particles such as fibrous particles, pollen, and drug particles in a human nasal cavity
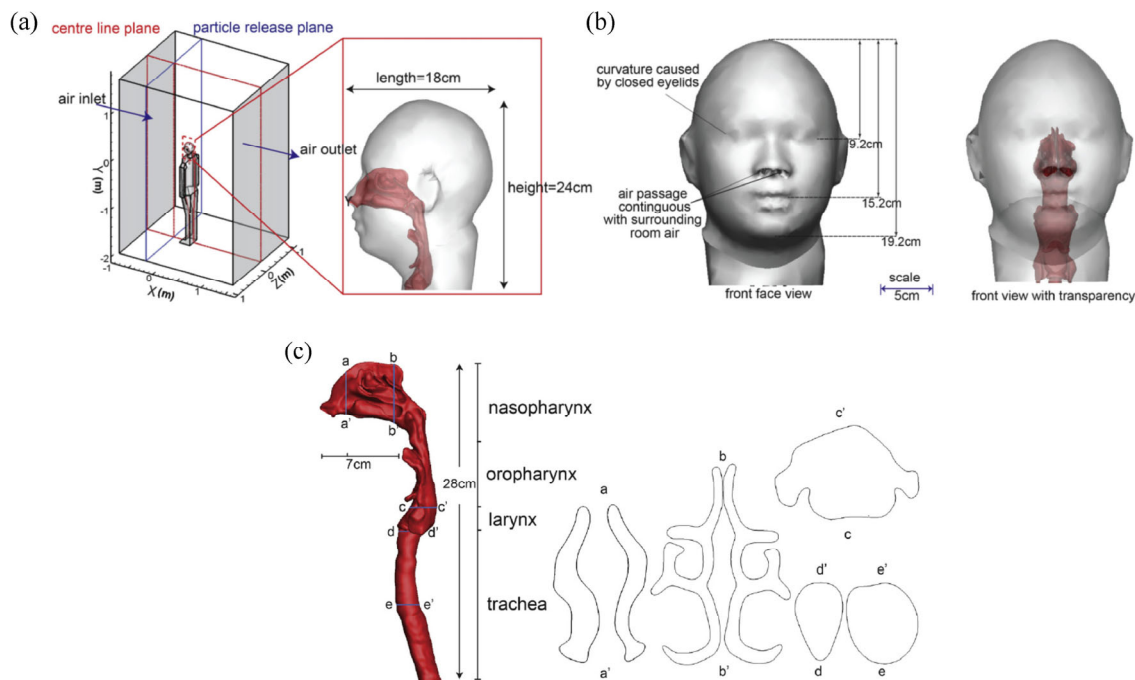

Fig. 15   (a) 3D CAD model incorporating the external surrounding room, human occupant, and the internal nasal-pharynx-larynx-trachea respiratory airway model. (b) Front view showing the detailed facial features. (c) Cross-sections labelled a–e taken at different locations within the internal upper respiratory airway which consists of the nasal cavity, pharynx, larynx, and trachea (Inthavong et al., 2012; reproduced with permission © Elsevier Ltd. 2012).

TSINGHUA UNIVERSITY PRESS   Springer
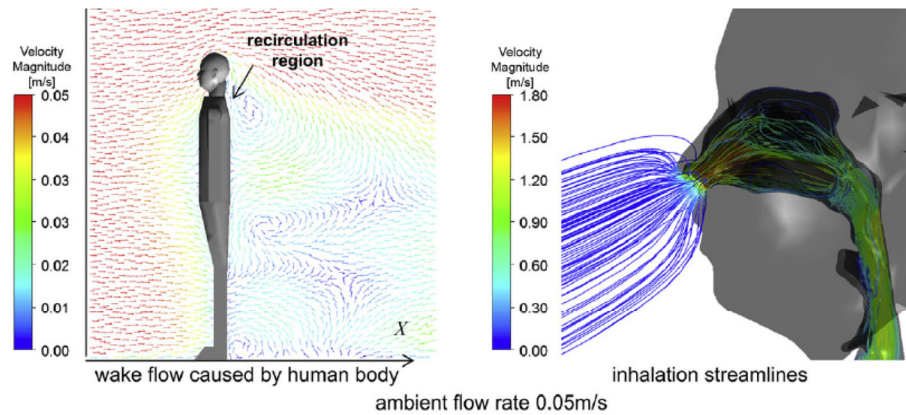
Fig. 16 Velocity vectors in the centreline plane showing the flow field around the humanoid (left). Streamlines showing the region of air that is inhaled through the nostrils and into the respiratory system (right). The inhalation rate of the nostrils is at 15 L/min (Inthavong et al., 2012; reproduced with permission © Elsevier Ltd. 2012).

(a) 1 μm particle deposition   (b) 15 μm particle deposition
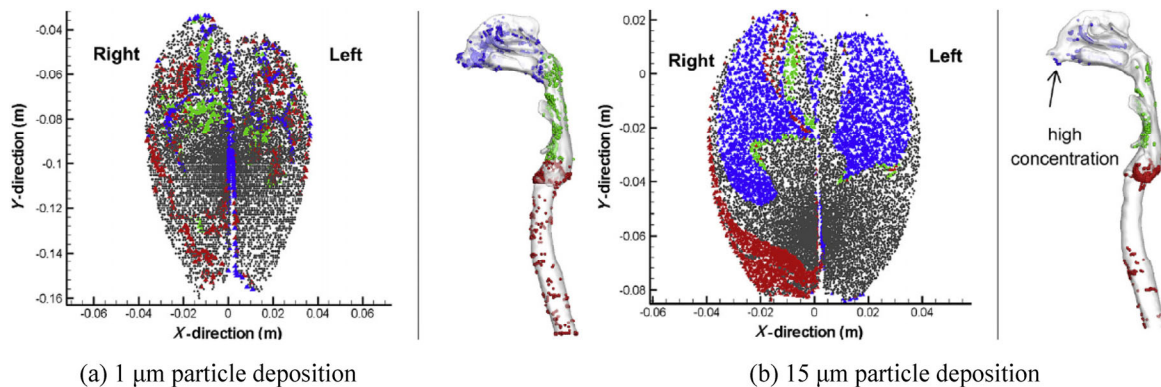
Fig. 17 Critical areas for the upstream particle release plane for inhaled particles and its deposition in the upper respiratory airway for ambient airflow rate of 0.05 m/s (Inthavong et al., 2012; reproduced with permission © Elsevier Ltd. 2012).

is treated differently to spherical particles. The main contributor to the change in dynamics is the drag coefficient. Studies of fibre deposition including asbestos or welding fumes are of interest because of its serious health consequences such as asbestosis and mesothelioma (Inthavong et al., 2008, 2013b).

The treatment of fibrous particles was evaluated by two methods using an elongated cylinder by Haider and Levenspiel (1989), or clusters of spherical aggregate particles (Tran-Cong et al., 2004). Haider and Levenspiel's (1989) model includes a shape factor (ratio of surface area of a sphere having the same volume as the fibre to surface area of the fibre), while Tran-Cong et al.'s (2004) model includes a volume equivalent diameter, a surface equivalent diameter, a shape factor called the "degree of circularity".

Normalisation of fibre deposition data is achieved through Stöber's (1972) correlations using an aerodynamic equivalent diameter and a dynamic shape factor. The dynamic shape factor provides a relationship for fibre length oriented perpendicular to the flow, and oriented parallel to the flow, and the aspect ratio (fibre length to the diameter). For spherical particles, Kelly et al. (2004) curve fitted their experimental data to provide a correlation predicting particle deposition efficiencies in the nasal cavity:

$$\eta = 1 - \exp\left(-\left(\alpha \cdot d_{\mathrm{ae}}^2 Q\right)^{\beta}\right) \qquad (9)$$

where $\alpha = 5.86 \times 10^{-5}$ and $\beta = 2.1892$. Combining Stöber's (1972) correlations with the inertial parameter, the same correlation to predict fibre deposition in the nasal cavity was formulated in Inthavong et al. (2008) with coefficients being $\alpha = 4.654 \times 10^{-5}$ and $\beta = 2.05$.

3.4 Submicron nanoparticle deposition

Transport of submicron and nanoparticles is mainly attributed to the Brownian diffusion behaviour, which increases as the nanoparticle size computational modelling of dilute suspensions of ultrafine and nano-scale particles decreases from 100 to 1 nm. The diffusion is caused by the Brownian force which is treated as an additional body force acting on the particle. It can be reconstructed from the diffusion coefficient D via the Einstein relation $F = kTU/D$, where U is the particle velocity, T is the temperature of the medium, and k is the Boltzmann constant.

The Eulerian multi-component mixture can be used to model the particle dispersion (Yu et al., 1998; Shi et al., 2006; Inthavong et al., 2011c). This involves treating the continuous (fluid) phase and the dilute (particle) phase as interpenetrating fields, where Brownian motion is driven by a concentration gradient and the diffusion coefficient, D dependent on each individual particle size is given as

$$D = \frac{kTC_c}{3\pi\mu d_p} \tag{10}$$

where C_c is the Cunningham correction factor, and μ is the fluid dynamic viscosity. This approach does not consider the particle inertia but provides simpler simulations and is efficient for a large number of particles.

The Lagrangian approach considers individual particle motion based on a force balance involving a variety of forces such as inertia, lift, thermophoretic and Brownian motion (Zamankhan et al., 2006; Longest and Xi, 2007). Since the Lagrangian approach equates the particle force balance equation of motion, then the time step becomes an important factor in different numerical integration schemes. To ensure accurate particle dispersion modelling, diffusional deposition results can be compared against its radial root mean square displacement. It was shown that a particle's Brownian dispersion was dependent on the computational mesh, and the integration time step for a given particle size, and that a mesh difference of 10× for the same geometry required time steps of 1 order of magnitude difference (Inthavong et al., 2016).

$$\sqrt{x^2} = \sqrt{(x(t) - x_0)^2} = \sqrt{2Dt} \tag{11}$$

A comparison of micron and submicron (nanoparticle) deposition using the Lagrangian approach shows the deposition efficiency over the range of 1–10000 nm or 1 nm to 10 μm was performed by Wang et al. (2009) and the results are shown in Fig. 18. Particle deposition in the nasal cavity was affected by particle size, flow rate, and to a less extent density.

For particles < 50 nm the rate of diffusion is inversely proportional to particle size, making the deposition mechanism diffusion dominant. Brownian motion is caused by collision of small particles by air molecules in the nasal cavity, and concentration gradients result in particle movement towards the nasal wall. Particles with a diameter in the size range of 0.05–1 μm have similar deposition efficiencies. For this particle range, all three deposition mechanisms, diffusion, inertial impaction, and sedimentation have an effect albeit on a smaller scale.

The inspiratory flow rate also has some effect on particle deposition. For micron particles, the total deposition efficiency increases with an increase in the flow rate. For
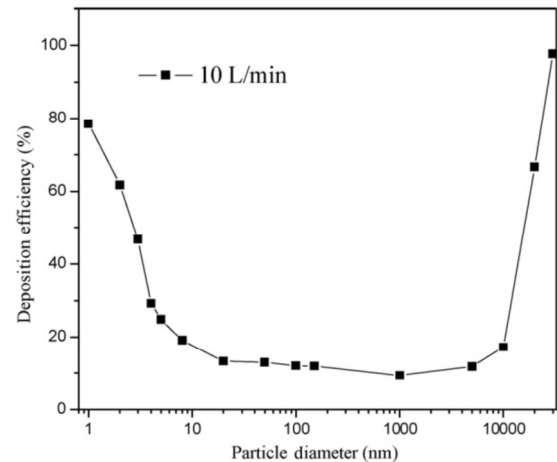

Fig. 18 Variations of particle deposition fraction vs. particle size in the nasal cavity at the inspiratory flow rate of 10 L/min.

nanoparticles less than 15 nm however, the efficiency decreases with an increase in the flow rate. The particle density is only significant for micron particles in its contribution to the particle inertia. Overall there is a difference in the local deposition patterns for micron and submicron particles. The significant regions of deposition for micron particles were found to be at the nasal valve and the middle septum parts in the nasal turbinate, and there is some difference in left and right cavities, while for submicron particles there was a uniform distribution of deposited particles.

3.5 Local regional deposition

Identifying local regional deposition within the nasal cavity provides the ability to predict the physiological outcomes. Important regions include the maxillary sinus and olfactory region.

The maxillary sinus is a major source of mucus production and susceptible to sinusitis during severe congestion. Micron particle deposition in the maxillary sinus is minimal because of the narrow ostia restricting flow to pass from the main nasal passage through the ostia and into the sinus (Xiong et al., 2008). Ultrafine particle (1–100 nm) motion is dominated by diffusion and their deposition onto its surrounding surfaces is reliant on low convection to diffusion ratio (i.e., Peclet number). If the flow rate through the nasal cavity is sufficiently low, the diffusion transport of ultrafine particles may be significant enough for the particles to pass into the paranasal sinuses. Ge et al. (2012) investigated local deposition fractions of ultrafine particles in a human sino-nasal cavity. The minimum ostium diameter was 4.6 and 3.78 mm, and the pressure difference between the ostium entrance and inside the maxillary sinus was 0.056 and 0.0026 Pa for the left and right chambers respectively (Fig. 19). The mass flow rate through the left and right
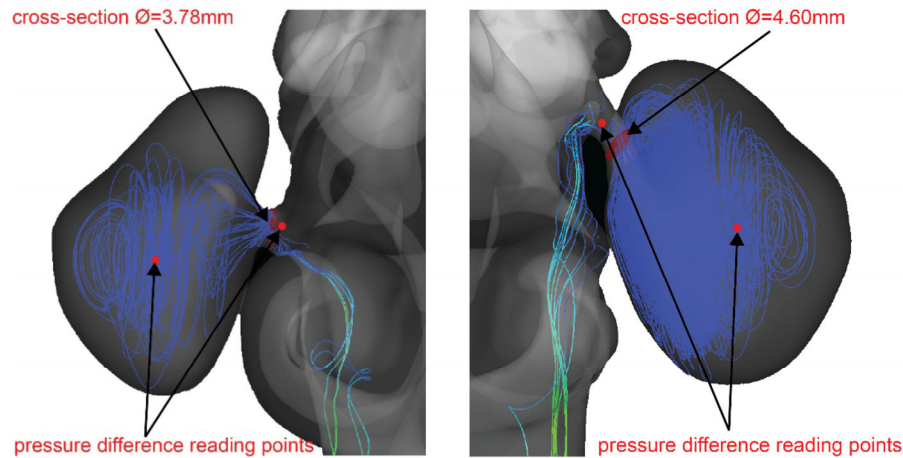
Fig. 19 Minimum ostium diameter shown in red cross-section plane was 4.6 and 3.78 mm, and the pressure difference between the ostium entrance and inside the maxillary sinus are 0.056 and 0.0026 Pa for the left and right sides respectively (Ge et al., 2012; reproduced with permission © Taylor & Francis 2012).

ostium is 11.4×10^{-9} and 6.77×10^{-9} kg/s which is < 0.006% of the total inhalation flow rate. This small percentage of flow is not conducive for convective transport of particles into the maxillary sinus and that if any deposition were to occur in this region, then it would be caused by Brownian diffusion.

Figure 20 shows the deposition of ultrafine particle deposition in the maxillary sinus for 1, 5, 10, 40, and 100 nm particles. There was no difference in deposition for 1 nm particle between a nasal cavity model with sinus (NC02-S) and without sinus (NC02) as both models predict near 100%. The difference in deposition efficiency between the two models at a flow rate of 4 L/min was most significant for 5 and 10 nm particles (17% and 16% difference respectively). As the particle size increased the difference between the two models diminished. For 1 nm particles, the difference was indiscernible since the deposition efficiency was already at 100%. While the quantifiable difference was not noticeable
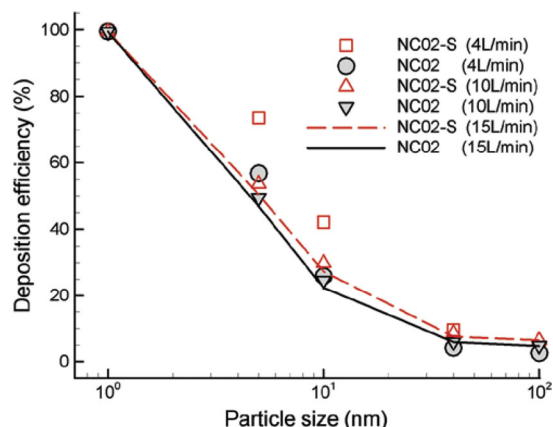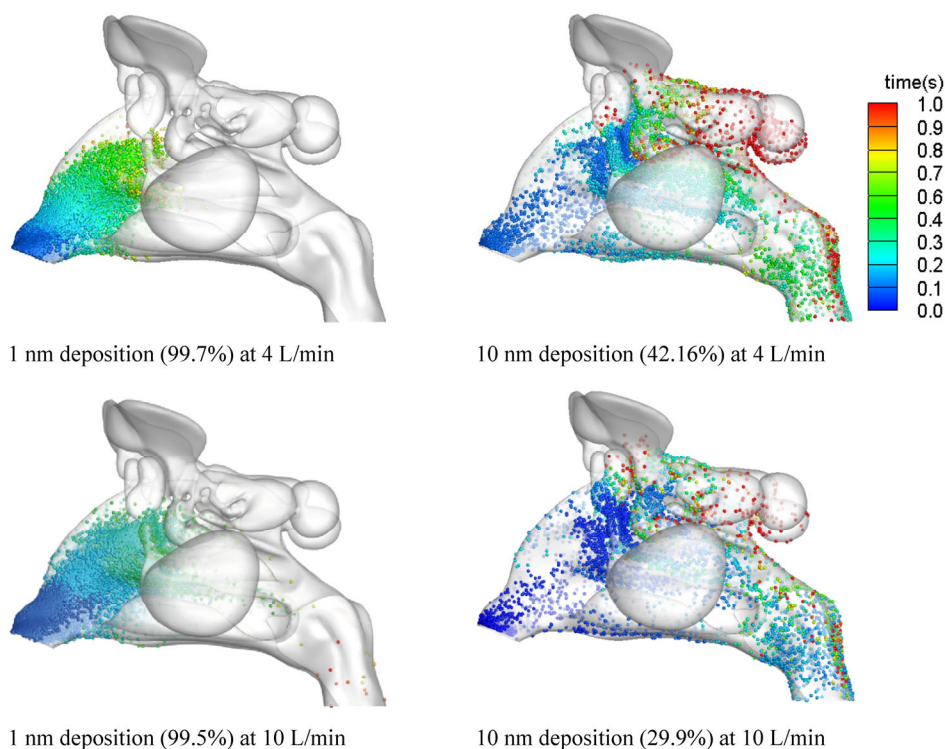

Fig. 20 Deposition efficiency comparison for nasal model with sinus NC02-S (red markers) and without sinus NC02 model (black markers) for 4, 10, and 15 L/min breathing rates (Ge et al., 2012; reproduced with permission © Taylor & Francis 2012).

it is expected that the 1 nm particle diffusion influence will be much stronger at the lower flow rate of 4 L/min, and that the deposition pattern locally will be different to that at a flow rate of 10 L/min.

Figure 21 shows the deposition distribution of 1 nm particles that earlier deposition occurs where a large proportion of the particles persist for less than 0.022 s in the nasal-sinus cavity. The strength or influence of the Brownian diffusion increases as the flow rate decreases, and at a flow rate of 4 L/min, deposition is found within the anterior half of the nasal-sinus cavity while at a flow rate 10 L/min deposition is a little more disperse with deposition sites found in the posterior half. The deposition pattern for 10 nm particles shows a more random and even distribution pattern. The residence time is 10× as great as that for 1 nm which suggests that the particles are transported with the inhaled flow field for longer and hence has the ability to travel deeper into the nasal cavity and perhaps down towards the lung region.

The particle residence time is important for NP deposition studies as it indicates the likelihood of deposition in different regions of the nasal cavity. For example, the shorter residence time of 1 nm means that deposition occurs nearly immediately and the deposition zone is restricted to the nasal cavity and further deposition downstream is unlikely. This protects the sensitive lung airways from those NPs that exhibit dangerous properties for respiratory health. Conversely the ability to deposit particles in the middle regions of the nasal cavity or even deeper into the lung airways with high deposition, can be important for therapeutic drug delivery.

The olfactory region contains layers of epithelial tissue of the mucous membranes, olfactory glands, neurons, and nerves. Recent findings of particle translocation to the brain have prompted research into the probability of inhalation

1 nm deposition (99.7%) at 4 L/min

10 nm deposition (42.16%) at 4 L/min

1 nm deposition (99.5%) at 10 L/min

10 nm deposition (29.9%) at 10 L/min

Fig. 21 NP deposition pattern in the nasal-sinus cavity for (a) 1 nm resulting in 98% deposition and (b) 10 nm resulting in 29.8% deposition. Particles are coloured by trajectory time within the nasal cavity before impacting onto the surfaces at 10 L/min (Ge et al., 2012; reproduced with permission © Taylor & Francis 2012).

exposure to olfactory deposition. Recent studies revealed that inhaled ultrafine solid particles could translocate into the brain by depositing on the olfactory mucosa and translocating along the olfactory nerve connected to the brain (Oberdörster et al., 2004). This has spawned strong interest in understanding the mechanics of olfactory particle deposition for both toxicology and medical applications.

Garcia et al. (2015) compared nanoparticle olfactory dose estimates between human and rat nasal models showing that deposition rates were lower in humans compared to rats. However, due to larger inhalation rates in humans, the olfactory dose per unit surface area was higher in humans in the 1–7 nm size range. Lower olfactory dose was also found in Dong et al. (2016), but it was reported that due to the inter-individual nasal anatomy variations, the precise olfactory deposition was difficult because the olfactory region was small, and slight variations in defining the olfactory region boundaries produced variations in the result.

Alternatively, the nose-to-brain route provides an attractive solution to directly deliver medication to the brain which can be used for the treatment of central nervous system-related disorders (Mistry et al., 2009), such as epileptic conditions, psychosis, and neurodegenerative disease. Dong et al. (2018) determined the initial particle locations leading to deposition in the olfactory region. For nasally administered medications, by naturally inhaling nano-

particles the initial locations for effective targeted drug delivery were provided. The particle deposition (Fig. 22) results showed that for olfactory targeted drug delivery, the particle initial positions needed to be within the inner superior corner of the nostril.

3.6 Visualising deposition and wall shear stress patterns

Representation of 3D results is limited to computational media that has ability to rotate the model to obtain the desired view. Even under this method, not all surfaces in a human nasal cavity can be viewed adequately, because of the many overlapping folds and curvatures in the geometry. An alternative is to transform the 3D model into a 2D representation by the *UV* mapping technique readily used in computer graphics. The letters *U* and *V* denote the coordinate axes of the transformed 2D plane while *X*, *Y*, *Z* are the coordinate axes of the 3D object. The 2D map provides an overview of the entire geometry, where both septal and lateral wall surfaces can be plotted simultaneously—a feature that is prohibitive in 3D models. The *UV* mapping is highly effective for reporting results in 2D format, e.g., paper reports.

Inthavong et al. (2014) proposed a workflow for converting the human nasal cavity into a 2D surface where the nasal cavity is firstly divided into the left and right
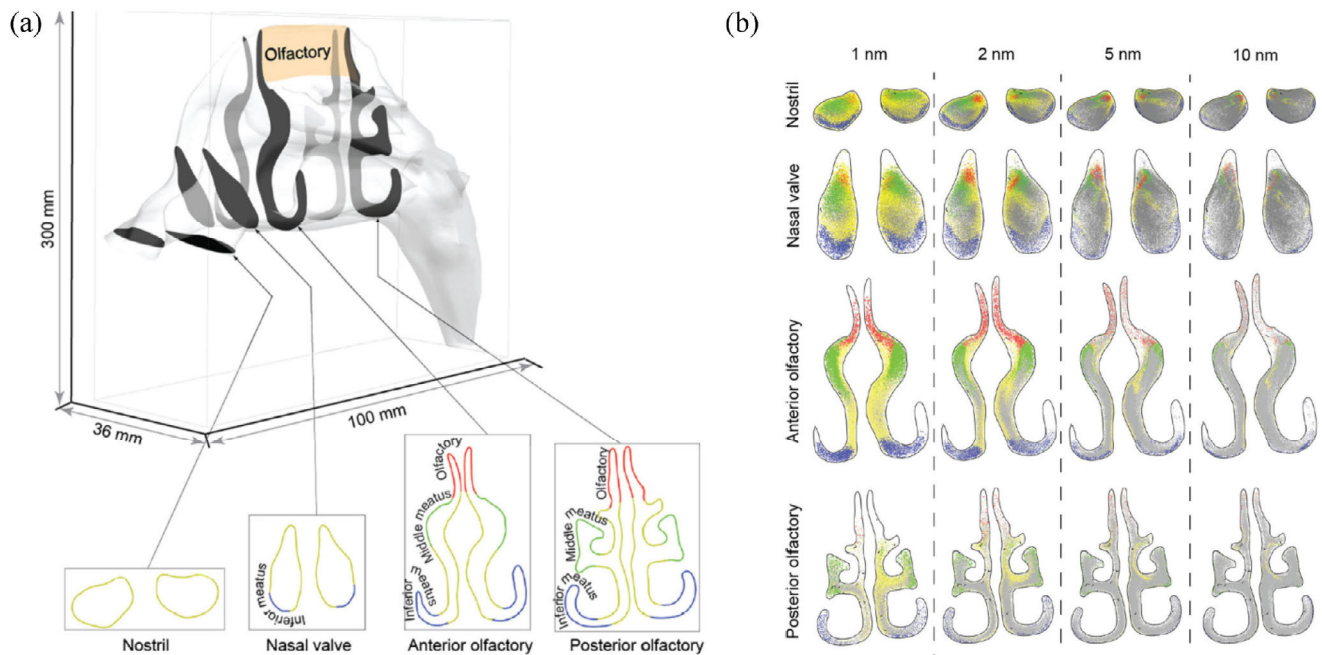
Fig. 22 (a) Nasal cavity model with four coronal slices and olfactory region. The coronal slice boundaries are coloured by the anatomy the slice passes through. (b) Particle locations at coronal slices, where coloured particles represent its eventual fate. Red = olfactory deposition; green = middle turbinate deposition; yellow = other nasal passage deposition; grey = escaped through pharynx. Flow rate was 5 L/min (Dong et al., 2018; reproduced with permission © Elsevier B.V. 2018).
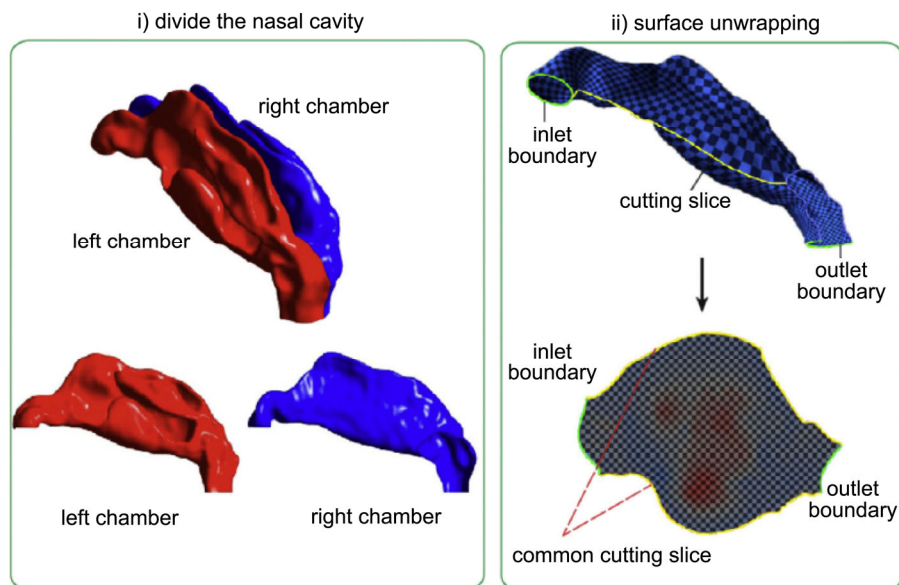

Fig. 23 Flow process in unwrapping the surface of a 3D model into a 2D domain. Characteristic lines are defined at the apex of the septum wall, middle meatus, and inferior meatus (Inthavong et al., 2014; reproduced with permission © Elsevier B.V. 2013).

chambers. Each chamber is then unwrapped by creating a cutting slice along the bottom of the geometry to create a common reference boundary which when unwrapped oppose each other separated by the wrapped surface. The common boundary is connected at either end by the inlet and outlet boundaries.

The 2D *UV* unwrapped model is normalized so that it the width and height are uniform so that any two nasal cavities that exhibit geometric differences can be directly compared. Figure 24 shows the differences in geometry shape from the 3D model to the 2D unwrapped model, and finally the normalized *UV* map. The vastly different geometry exhibited by the rat nasal cavity can also be normalized for direct comparison.

TSINGHUA UNIVERSITY PRESS | Springer
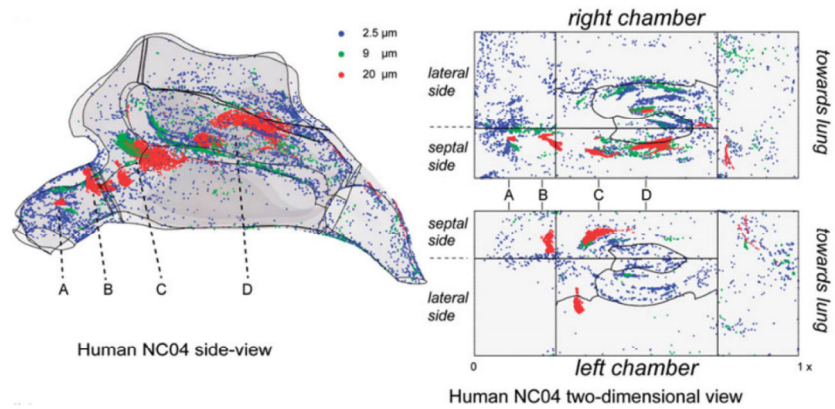
(a) human nasal cavity model-NC04
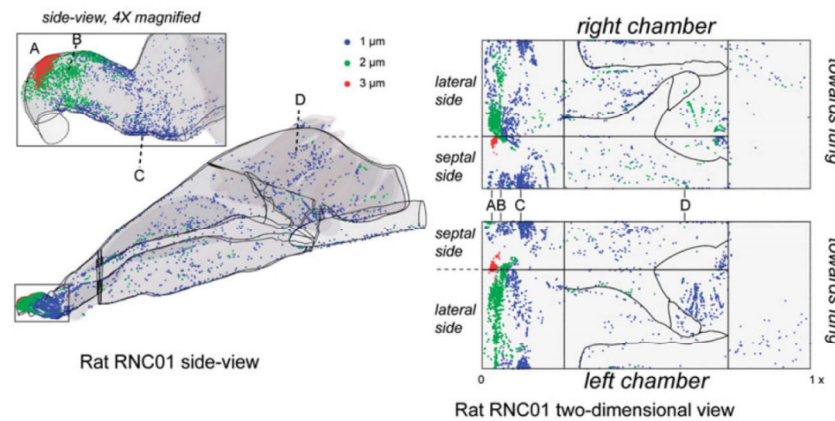
(b) rat nasal cavity model-RNC01

Fig. 24 Normalization of the coordinates U and V of the two different nasal cavities (human model NC04 and rat model RNC01) that have been unwrapped and normalized. (a) and (b) show particle deposition locations (Shang et al., 2015a; reproduced with permission © Taylor & Francis 2015).

4 Future work

Complex models incorporating multiphysics will continue to push the current capabilities into new frontiers, supported by advanced physics modelling and readily available computational resources. For example, an integrated model encompassing the respiratory airway from outer nose down to lung regions can provide a more holistic description of inhaled particles and its eventual fate in the respiratory airway (Fig. 25). Transient flow modelling coupled with
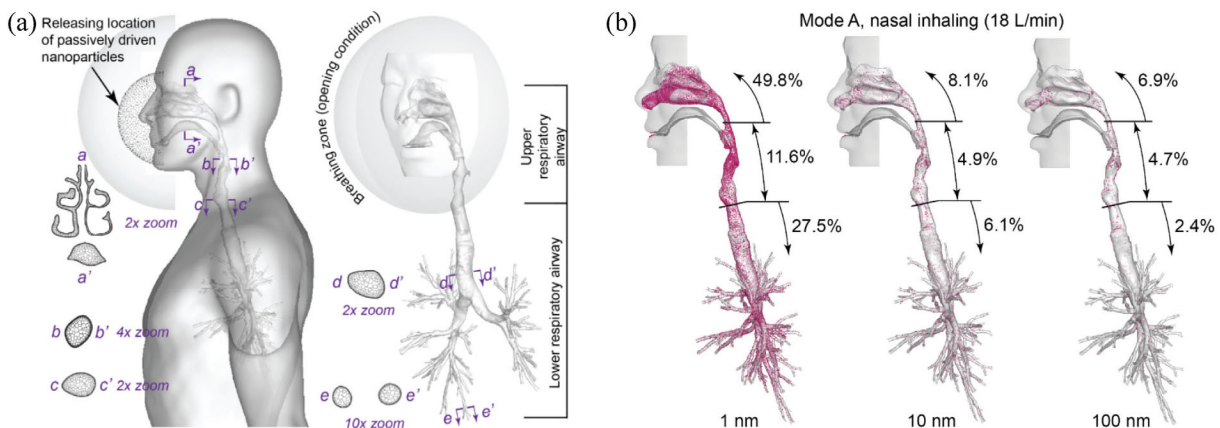
Fig. 25 (a) Reconstructed pulmonary airway model and interior polyhedral mesh configurations at selected slices. (b) Deposition fraction comparison of 1, 10, 100 nm particles under Mode A (inhaling via nose only at flow rate of 18 L/min) (Dong et al., 2019; reproduced with permission © John Wiley & Sons, Ltd. 2019).

fluid-structure-interactions or at least moving (dynamic) mesh motion can replicate the dynamic states of physiological motion in the nasal cavity. Application of elastic surfaces is essential for understanding the influence, and effective treatment of nasal valve collapse and to a less extent collapse of the alae nasi.

Particle interaction with the mucus layer provides further analysis of the eventual toxicology effect of inhaled particles, based on its deposition rate. This accounts for the mucociliary clearance to determine eventual deposition penetration into the mucus, providing detailed information to physiologically based pharmacokinetic (PBPK) models. The nose's mucociliary function serves as a defence mechanism that offers a pathway for possible particle translocation or eventual dissolution into the mucus sublayers. Recently, Rygg and Longest (2016) and later Shang et al. (2019) have both provided new methods for modelling the mucus motion and its influence on clearance mechanisms.

The emergence of machine learning and its application to CFD results can produce rapid results, through the artificial neural network (ANN) technique. Such methods are useful in providing insight into modelling the spread of fire in buildings. Its application to particle dispersion, and pollutant exposure to the respiratory airway has yet to be studied. In addition to speeding up simulations, the fast fluid dynamics (FFD) technique has seen progress, and convergence of machine learning with FFD can produce the next wave of modelling capability.

Optimised and personalised health care will rely on massive data (e.g., big data concept) leading to the next revolution in health care in the so-called digital twin. This term refers to the digital representation of a physical product such as the human anatomy. Along with the developments of the internet of things (IoT), digital twin is becoming a potential across many industries, including healthcare, and it is expected that with machine learning, this will become a reality. However, its success will rely on large data sets and well-established results to ensure the computational analysis provide reliable results.

5 Conclusions

The computer-aided engineering field is experiencing a huge explosion in modelling capability and available resources. This provides an excellent opportunity for researchers to expand on the current state-of-the-art modelling work. Studies of indoor air quality and its effect on respiratory health were reviewed through a multiphase flow journey of the particle dynamics and its trajectory from inside a room, as it enters the nostrils, and its eventual deposition in the respiratory airway. Research outcomes were presented which showed how an integrated model combining the outer

surrounding air environment can be included with an in-silico human model with its respiratory anatomy. The future of computational inhaled particles has substantial potential through the available computational resources and advanced models that will bring new opportunities in the computational modelling industry.

References

Aitken, R. J., Baldwin, P. E. J., Beaumont, G. C., Kenny, L. C., Maynard, A. D. 1999. Aerosol inhalability in low air movement environments. *J Aerosol Sci*, 30: 613–626.

Anderson, K. R., Anthony, T. R. 2014. Influence of secondary aspiration on human aspiration efficiency. *J Aerosol Sci*, 75: 65–80.

Anthony, T. R. 2010. Contribution of facial feature dimensions and velocity parameters on particle inhalability. *Ann Occup Hyg*, 54: 710–725.

Anthony, T. R., Anderson, K. R. 2013. Computational fluid dynamics investigation of human aspiration in low-velocity air: Orientation effects on mouth-breathing simulations. *Ann Occup Hyg*, 57: 740–757.

Anthony, T. R., Flynn, M. R. 2006. Computational fluid dynamics investigation of particle inhalability. *J Aerosol Sci*, 37: 750–765.

Baldwin, P. E. J., Maynard, A. D. 1998. A survey of wind speeds in indoor workplaces. *Ann Occup Hyg*, 42: 303–313.

Belyaev, S. P., Levin, L. M. 1972. Investigation of aerosol aspiration by photographing particle tracks under flash illumination. *J Aerosol Sci*, 3: 127–140.

Chen, F. Z., Yu, S. C. M., Lai, A. C. K. 2006. Modeling particle distribution and deposition in indoor environments with a new drift–flux model. *Atmos Environ*, 40: 357–367.

Chen, Q. 1995. Comparison of different k–ε models for indoor air flow computations. *Numer Heat Tr B: Fund*, 28: 353–369.

Cheong, K. W., Djunaedy, E. 2001. The influence of furniture and equipment layouts on airflow pattern in a clean room. *Build Serv Eng Res T*, 22: 261–266.

Choi, J. I., Edwards, J. R. 2012. Large-eddy simulation of human-induced contaminant transport in room compartments. *Indoor Air*, 22: 77–87.

Churchill, S. E., Shackelford, L. L., Georgi, J. N., Black, M. T. 2004. Morphological variation and airflow dynamics in the human nose. *Am J Hum Biol*, 16: 625–638.

Dai, Y.-T., Juang, Y.-J., Wu, Y.-Y., Breysse, P. N., Hsu, D.-J. 2006. *In vivo* measurements of inhalability of ultralarge aerosol particles in calm air by humans. *J Aerosol Sci*, 37: 967–973.

Dehbi, A. 2011. Prediction of extrathoracic aerosol deposition using RANS-Random Walk and LES approaches. *Aerosol Sci Tech*, 45: 555–569.

Dong, J., Shang, Y., Tian, L., Inthavong, K., Qiu, D., Tu, J. 2019. Ultrafine particle deposition in a realistic human airway at multiple inhalation scenarios. *Int J Numer Meth Biomed Engng*, 35: e3215.

Dong, J. L., Shang, Y. D., Inthavong, K., Chan, H.-K., Tu, J. Y. 2018. Partitioning of dispersed nanoparticles in a realistic nasal passage for targeted drug delivery. *Int J Pharmaceut*, 543: 83–95.

Dong, J. L., Shang, Y. D., Inthavong, K., Tu, J. Y., Chen, R., Bai, R., Wang, D. L., Chen, C. Y. 2016. From the cover: comparative numerical modeling of inhaled nanoparticle deposition in human and rat nasal cavities. *Toxicol Sci*, 152: 284–296.

Doorly, D. J., Taylor, D. J., Schroter, R. C. 2008. Mechanics of airflow in the human nasal airways. *Resp Physiol Neurobi*, 163: 100–110.

Edge, B. A., Paterson, E. G., Settles, G. S. 2005. Computational study of the wake and contaminant transport of a walking human. *J Fluid Eng*, 127: 967–977.

Garcia, G. J. M., Schroeter, J. D., Kimbell, J. S. 2015. Olfactory deposition of inhaled nanoparticles in humans. *Inhal Toxicol*, 27: 394–403.

Ge, Q. J., Inthavong, K., Tu, J. Y. 2012. Local deposition fractions of ultrafine particles in a human nasal-sinus cavity CFD model. *Inhal Toxicol*, 24: 492–505.

Ghahramani, E., Abouali, O., Emdad, H., Ahmadi, G. 2014. Numerical analysis of stochastic dispersion of micro-particles in turbulent flows in a realistic model of human nasal/upper airway. *J Aerosol Sci*, 67: 188–206.

Haider, A., Levenspiel, O. 1989. Drag coefficient and terminal velocity of spherical and nonspherical particles. *Powder Technol*, 58: 63–70.

Heschl, C., Inthavong, K., Sanz, W., Tu, J. 2014. Nonlinear eddy viscosity modeling and experimental study of jet spreading rates. *Indoor Air*, 24: 93–102.

Heschl, C., Inthavong, K., Sanz, W., Tu, J. Y. 2013. Evaluation and improvements of RANS turbulence models for linear diffuser flows. *Comput Fluids*, 71: 272–282.

Holmberg, S., Chen, Q. 2003. Air flow and particle control with different ventilation systems in a classroom. *Indoor Air*, 13: 200–204.

Inthavong, K., Ge, Q. J., Li, X. D., Tu, J. Y. 2012. Detailed predictions of particle aspiration affected by respiratory inhalation and airflow. *Atmos Environ*, 62: 107–117.

Inthavong, K., Ge, Q. J., Li, X. D., Tu, J. Y. 2013a. Source and trajectories of inhaled particles from a surrounding environment and its deposition in the respiratory airway. *Inhal Toxicol*, 25: 280–291.

Inthavong, K., Ge, Q. J., Se, C. M. K., Yang, W., Tu, J. Y. 2011a. Simulation of sprayed particle deposition in a human nasal cavity including a nasal spray device. *J Aerosol Sci*, 42: 100–113.

Inthavong, K., Ma, J., Shang, Y., Dong, J., Chetty, A. S. R., Tu, J., Frank-Ito, D. 2019. Geometry and airflow dynamics analysis in the nasal cavity during inhalation. *Clin Biomech*, 66: 97–106.

Inthavong, K., Mouritz, A. P., Dong, J. L., Tu, J. Y. 2013b. Inhalation and deposition of carbon and glass composite fibre in the respiratory airway. *J Aerosol Sci*, 65: 58–68.

Inthavong, K., Shang, Y. D., Tu, J. Y. 2014. Surface mapping for visualization of wall stresses during inhalation in a human nasal cavity. *Resp Physiol Neurobi*, 190: 54–61.

Inthavong, K., Tao, Y., Petersen, P., Mohanarangam, K., Yang, W., Tu, J. Y. 2017. A smoke visualisation technique for wake flow from a moving human manikin. *J Visual*, 20: 125–137.

Inthavong, K., Tian, L., Tu, J. Y. 2016. Lagrangian particle modelling of spherical nanoparticle dispersion and deposition in confined flows. *J Aerosol Sci*, 96: 56–68.

Inthavong, K., Tian, Z. F., Li, H. F., Tu, J. Y., Yang, W., Xue, C. L., Li, C. G. 2006. A numerical study of spray particle deposition in a human nasal cavity. *Aerosol Sci Tech*, 40: 1034–1045.

Inthavong, K., Tu, J. Y., Heschl, C. 2011b. Micron particle deposition in the nasal cavity using the v^2–f model. *Comput Fluids*, 51: 184–188.

Inthavong, K., Wen, J., Tian, Z. F., Tu, J. Y. 2008. Numerical study of fibre deposition in a human nasal cavity. *J Aerosol Sci*, 39: 253–265.

Inthavong, K., Zhang, K., Tu, J. Y. 2011c. Numerical modelling of nanoparticle deposition in the nasal cavity and the tracheobronchial airway. *Computer Methods in Biomechanics and Biomedical Engineering*, 14: 633–643.

Kelly, J. T., Asgharian, B., Kimbell, J. S., Wong, B. A. 2004. Particle deposition in human nasal airway replicas manufactured by different methods. Part II: Ultrafine particles. *Aerosol Sci Tech*, 38: 1072–1079.

Kennedy, N. J., Hinds, W. C. 2002. Inhalability of large solid particles. *J Aerosol Sci*, 33: 237–255.

Kim, T., Flynn, M. R. 1991. Airflow pattern around a worker in a uniform freestream. *Am Ind Hyg Assoc J*, 52: 287–296.

King Se, C. M., Inthavong, K., Tu, J. Y. 2010. Inhalability of micron particles through the nose and mouth. *Inhal Toxicol*, 22: 287–300.

Kulmala, I., Säämänen, A., Enbom, S. 1996. The effect of contaminant source location on worker exposure in the near-wake region. *Ann Occup Hyg*, 40: 511–523.

Lai, A., Nazaroff, W. 2005. Supermicron particle deposition from turbulent chamber flow onto smooth and rough vertical surfaces. *Atmos Environ*, 39: 4893–4900.

Li, K. Q., Gong, G. C. 2012. Numerical simulation of indoor suspension particles based on v2-F model. *Appl Math Model*, 36: 2510–2520.

Li, X. D., Inthavong, K., Tu, J. Y. 2012. Particle inhalation and deposition in a human nasal cavity from the external surrounding environment. *Build Environ*, 47: 32–39.

Liu, S. C., Novoselac, A. 2014. Lagrangian particle modeling in the indoor environment: A comparison of RANS and LES turbulence methods (RP-1512). *HVAC&R Res*, 20: 480–495.

Liu, Y., Matida, E. A., Gu, J. J., Johnson, M. R. 2007. Numerical simulation of aerosol deposition in a 3-D human nasal cavity using RANS, RANS/EIM, and LES. *J Aerosol Sci*, 38: 683–700.

Longest, P. W., Xi, J. X. 2007. Effectiveness of direct Lagrangian tracking models for simulating nanoparticle deposition in the upper airways. *Aerosol Sci Tech*, 41: 380–397.

Luongo, J. C., Fennelly, K. P., Keen, J. A., Zhai, Z. J., Jones, B. W., Miller, S. L. 2016. Role of mechanical ventilation in the airborne transmission of infectious agents in buildings. *Indoor Air*, 26: 666–678.

Mistry, A., Stolnik, S., Illum, L. 2009. Nanoparticles for direct nose-to-brain delivery of drugs. *Int J Pharmaceut*, 379: 146–157.

Murakami, S. 1992. Diffusion characteristics of airborne particles with gravitational setting in an convection-dominant indoor flow field. *ASHRAE Transactions*, 98: 82–97.

Murakami, S. 2004. Analysis and design of micro-climate around the human body with respiration by CFD. *Indoor Air*, 14: 144–156.

Nazaroff, W. W. 2008. Inhalation intake fraction of pollutants from episodic indoor emissions. *Build Environ*, 43: 269–277.

Nielsen, P. B., Kato, S., Chen, Q. 1998. The selection of turbulence models for prediction of room airflow. *ASHRAE Transactions*, 104: 1119–1127.

Oberdörster, G., Sharp, Z., Atudorei, V., Elder, A., Gelein, R., Kreyling, W., Cox, C. 2004. Translocation of inhaled ultrafine particles to the brain. *Inhal Toxicol*, 16: 437–445.

Oberoi, R. C., Choi, J.-I., Edwards, J. R., Rosati, J. A., Thornburg, J., Rodes, C. E. 2010. Human-induced particle Re-suspension in a room. *Aerosol Sci Tech*, 44: 216–229.

Poussou, S. B., Mazumdar, S., Plesniak, M. W., Sojka, P. E., Chen, Q. Y. 2010. Flow and contaminant transport in an airliner cabin induced by a moving body: Model experiments and CFD predictions. *Atmos Environ*, 44: 2830–2839.

Rygg, A., Longest, P. W. 2016. Absorption and clearance of pharmaceutical aerosols in the human nose: Development of a CFD model. *J Aerosol Med Pulm D*, 29: 416–431.

Shang, Y. D., Dong, J. L., Inthavong, K., Tu, J. Y. 2015a. Comparative numerical modeling of inhaled micron-sized particle deposition in human and rat nasal cavities. *Inhal Toxicol*, 27: 694–705.

Shang, Y. D., Inthavong, K., Tu, J. Y. 2015b. Detailed micro-particle deposition patterns in the human nasal cavity influenced by the breathing zone. *Comput Fluids*, 114: 141–150.

Shang, Y., Inthavong, K., Tu, J. 2019. Development of a computational fluid dynamics model for mucociliary clearance in the nasal cavity. *J Biomech*, 85: 74–83.

Shi, H., Kleinstreuer, C., Zhang, Z. 2006. Laminar airflow and nano-particle or vapor deposition in a human nasal cavity model. *J Biomech Eng*, 128: 697–706.

Sleeth, D. K., Vincent, J. H. 2009. Inhalability for aerosols at ultra-low windspeeds. *J Phys: Conf Ser*, 151: 012062.

Stöber, W. 1972. Dynamic shape factors of nonspherical aerosol particles. In: *Assessment of Airborne Particles*. Charles Thomas: 249–289.

Tao, Y., Inthavong, K., Tu, J. Y. 2017a. Computational fluid dynamics study of human-induced wake and particle dispersion in indoor environment. *Indoor Built Environ*, 26: 185–198.

Tao, Y., Inthavong, K., Tu, J. Y. 2017b. Dynamic meshing modelling for particle resuspension caused by swinging manikin motion. *Build Environ*, 123: 529–542.

Tao, Y., Inthavong, K., Tu, J. Y. 2017c. A numerical investigation of wind environment around a walking human body. *J Wind Eng Ind Aerod*, 168: 9–19.

Taylor, D. J., Doorly, D. J., Schroter, R. C. 2010. Inflow boundary profile prescription for numerical simulation of nasal airflow. *J Roy Soc Interface*, 7: 515–527.

Thatcher, T. L., Wilson, D. J., Wood, E. E., Craig, M. J., Sextro, R. G. 2004. Pollutant dispersion in a large indoor space: Part 1—Scaled experiments using a water-filled model with occupants and furniture. *Indoor Air*, 14: 258–271.

Tran-Cong, S., Gay, M., Michaelides, E. E. 2004. Drag coefficients of irregularly shaped particles. *Powder Technol*, 139: 21–32.

Wang, J. L., Chow, T.-T. 2011. Numerical investigation of influence of human walking on dispersion and deposition of expiratory droplets in airborne infection isolation room. *Build Environ*, 46: 1993–2002.

Wang, S. M., Inthavong, K., Wen, J., Tu, J. Y., Xue, C. L. 2009. Comparison of micron- and nanoparticle deposition patterns in a realistic human nasal cavity. *Resp Physiol Neurobi*, 166: 142–151.

Whicker, J. J., Wasiolek, P. T., Tavani, R. A. 2002. Influence of room geometry and ventilation rate on airflow and aerosol dispersion: implications for worker protection. *Health Phys*, 82: 52–63.

Xi, J. X., Kim, J., Si, X. A. 2016. Effects of nostril orientation on airflow dynamics, heat exchange, and particle depositions in human noses. *Eur J Mech B-Fluid*, 55: 215–228.

Xiong, G. X., Zhan, J. M., Zuo, K. J., Li, J. F., Rong, L. W., Xu, G. 2008. Numerical flow simulation in the post-endoscopic sinus surgery nasal cavity. *Med Biol Eng Comput*, 46: 1161–1167.

Yu, G., Zhang, Z., Lessmann, R. 1998. Fluid flow and particle diffusion in the human upper respiratory system. *Aerosol Sci Tech*, 28: 146–158.

Zamankhan, P., Ahmadi, G., Wang, Z., Hopke, P. K., Cheng, Y.-S., Chung Su, W., Leonard, D. 2006. Airflow and deposition of nano-particles in a human nasal cavity. *Aerosol Sci Tech*, 40: 463–476

Zhang, Z., Chen, Q. 2009. Prediction of particle deposition onto indoor surfaces by CFD with a modified Lagrangian method. *Atmos Environ*, 43: 319–328.

Zhang, Z., Zhang, W., Zhai, Z. J., Chen, Q. Y. 2007. Evaluation of various turbulence models in predicting airflow and turbulence in enclosed environments by CFD: Part 2—comparison with experimental data from literature. *HVAC&R Res*, 13: 871–886.